Applied Physics Letters

A "Janus" double sided mid-IR photodetector based on a MIM architecture

Cite as: Appl. Phys. Lett. **119**, 181102 (2021); https://doi.org/10.1063/5.0065591
Submitted: 17 August 2021 • Accepted: 16 October 2021 • Published Online: 01 November 2021

Mario Malerba, Mathieu Jeannin, Stefano Pirotta, et al.

View Online Export Citation CrossMark

ARTICLES YOU MAY BE INTERESTED IN

Exciton-polaritons in GaAs-based slab waveguide photonic crystals
Applied Physics Letters **119**, 181101 (2021); https://doi.org/10.1063/5.0071248

Optomechanical temporal sampling of terahertz signals
Applied Physics Letters **119**, 181103 (2021); https://doi.org/10.1063/5.0068852

The challenge of tuning the ratio of lattice/total thermal conductivity toward conversion efficiency vs power density
Applied Physics Letters **119**, 180501 (2021); https://doi.org/10.1063/5.0071039

© 2021 Author(s).

Applied Physics Letters ARTICLE scitation.org/journal/apl

A "Janus" double sided mid-IR photodetector based on a MIM architecture

Cite as: Appl. Phys. Lett. **119**, 181102 (2021); doi: 10.1063/5.0065591
Submitted: 17 August 2021 · Accepted: 16 October 2021 ·
Published Online: 1 November 2021

View Online Export Citation CrossMark

Mario Malerba,[1,a)] Mathieu Jeannin,[1] Stefano Pirotta,[1] Lianhe Li,[2] Alexander Giles Davies,[2] Edmund Linfield,[2] Adel Bousseksou,[1] Jean-Michel Manceau,[1] and Raffaele Colombelli[1,a)]

AFFILIATIONS

[1]Centre de Nanosciences et de Nanotechnologies (C2N), CNRS UMR 9001, Université Paris-Saclay, 91120 Palaiseau, France
[2]School of Electronic and Electrical Engineering, University of Leeds, Woodhouse Lane, Leeds LS2 9JT, United Kingdom

[a)]**Authors to whom correspondence should be addressed:** mario.malerba@c2n.upsaclay.fr and raffaele.colombelli@c2n.upsaclay.fr

ABSTRACT

We present a mid-IR ($\lambda \sim 8.3\ \mu$m) quantum well infrared photodetector (QWIP) fabricated on a mid-IR transparent substrate, allowing photodetection with illumination from either the front surface or through the substrate. The device is based on a 400 nm-thick GaAs/AlGaAs semiconductor QWIP heterostructure enclosed in a nanostructured metal–insulator–metal cavity and hosted on a mid-IR transparent ZnSe substrate. Metallic stripes are symmetrically patterned by e-beam lithography on both sides of the active region. The detector spectral coverage spans from $\lambda \sim 7.15$ to $\lambda \sim 8.7\ \mu$m by changing the stripe width L—from $L = 1.0$ to $L = 1.3\ \mu$m—thus frequency-tuning the optical cavity mode. Both micro-FTIR passive optical characterizations and photocurrent measurements of the two-port system are carried out. They reveal a similar spectral response for the two detector ports with an experimentally measured T_{BLIP} of ~200 K.

Published under an exclusive license by AIP Publishing. https://doi.org/10.1063/5.0065591

Quantum well infrared photodetectors (QWIPs) are among the most suitable detectors for imaging, high speed, and/or heterodyne detection in the mid-infrared spectral range (mid-IR, $\lambda = 3$–$30\ \mu$m). Applications cover trace gas detection, atmospheric studies or space science, IR imaging, and free-space optical communications.[1–4] They combine a high sensitivity akin to mercury cadmium telluride (MCT) or InSb detectors with an ultrafast intrinsic response time.[5] Recently, the use of resonant metallic cavities has both enhanced their sensitivity and allowed room-temperature operation at the long wavelength end of the mid-IR spectral range.[4,6,7] Their large electronic bandwidth makes them also excellent candidates for mid-IR cameras.

Despite a wide variety of coupling schemes and confinement strategies,[8–13] each specifically optimized on the heterostructure characteristics (e.g., the semiconductor thickness), to date, the state of the art performance is obtained in cavity-embedded QWIPs, based on metal–insulator–metal (MIM) architectures that enclose the active region between a continuous metallic plane and patterned metallic nanostructures. In comparison with other coupling mechanisms, employing metallic or dielectric nanostructured architectures, these MIM cavities—optimized for thin heterostructures—ensure a maximal electromagnetic overlap between incoming radiation and the active region and naturally satisfy the ISB transition selection rule. The continuous metallic plane is a technological requirement originating from the fabrication procedure of the device, relying up to now on Au–Au thermocompression wafer bonding. It presents two main drawbacks: (i) it induces additional parasitic capacitances reducing the electronic bandwidth of the detectors,[6] and (ii) it blocks optical access from the backside of the sample. While the first drawback has recently been circumvented using fabrication-intensive dry-etching techniques, the second one is by design impossible to avoid. Recently, in view of developing cavity-enhanced intersubband (ISB) devices, original metal–metal architectures that enable bonding on arbitrary, potentially transparent substrates have been introduced[13] and also 3D structuring of the semiconductor active region.[14–16]

In this Letter, we present a mid-IR QWIP based on metallic microcavities symmetrically patterned on both sides of the semiconductor heterostructure and fabricated on a mid-IR transparent ZnSe substrate. It permits detection with illumination from both sides of the device and—potentially—visible illumination from the backside (ZnSe is transparent for visible wavelengths larger than 500 nm). We first optically characterize the device and show that absorption within the optical cavity exhibits the same spectral features, as expected, of a system on a continuous metallic ground plane and then we measure the current–voltage characteristics and the photocurrent response for

Published under an exclusive license by AIP Publishing

different cavity resonance frequencies and different temperatures. Our architecture is directly compatible with the integration of RF coplanar lines without having to etch through a thick metallic layer.[4] It has a clear potential for heterodyne applications, where collinear alignment between the local oscillator and the input signal beams can be difficult or unwanted.[17] The efficient backside injection of the local oscillator beam allows an independent optical path for the signal beam impinging on the device from the front side. Finally, it enables the integration with high-speed, chip level, multiplexed electronic readout circuits toward compact, high resolution, ultrasensitive, and ultrafast mid-IR cameras. The QWIP active region is composed of eight periods of epitaxially grown square quantum wells ($Al_{0.25}Ga_{0.75}As$/GaAs 25/5.2 nm), Si-doped to a nominal $n_{2D} = 3 \times 10^{11}$ cem^{-2} and designed to operate around $\lambda = 8.4\,\mu$m (heterostructure design adapted from Ref. 6). The active region is embedded between contact layers (50 and 100 nm of GaAs doped to a nominal $n_{3D} = 4 \times 10^{18}$ cm^{-3}, as top and bottom contacts, respectively) and is separated from the GaAs wafer by a 400 nm-thick $Al_{0.60}Ga_{0.40}As$ etch-stop layer. Figure 1(a) describes the device fabrication.

It consists of a first patterning/metal evaporation step, followed by the transfer of the AR from its original substrate to a new mid-IR transparent host, a second aligned patterning/metal deposition step, and final dry-etching, which defines the structures vertically. In detail, a first electron beam lithography (EBL) is performed on the native sample to define stripes of width L spanning between 0.9 and 1.35 μm with a fixed period $P = 4\,\mu$m, on areas of approximately $80 \times 80\ \mu$m^2 [Figs. 1(b) and 1(c)]. Next, titanium and gold (5/150 nm) are evaporated and lifted off, forming the first metal/semiconductor contact. A further step of optical lithography is carried out to connect all the devices to a common "ground" bonding pad. A Ti/Au/Ti (5/200/20 nm) stack is evaporated and lifted off. The final 20 nm thick Ti layer is used to enhance the adhesion strength of the metallic pads in the following step. The sample is then flipped and bonded to a host 1-mm-thick, optical-grade-polished ZnSe substrate using a commercial epoxy (Epotek 353ND). The native GaAs substrate is then selectively etched in a citric acid solution until the $Al_{0.6}Ga_{0.4}As$ etch stop layer. The latter is removed in HF, exposing the pristine doped layer. A second EBL lithography is performed with a careful alignment of the same design on the previous pattern, followed by Ti/Au (5/150 nm) metal evaporation. We estimate the lateral alignment error to be around 20 nm. A final photolithography and metallization carried out to define individual bonding pads, allowing each device to be electrically addressed and measured as a single detecting "pixel." The non-metallized, exposed semiconductor regions are finally etched in a RIE-ICP reactor using a $SiCl_4$/Ar plasma, using the gold pattern/contacts as a mask. Finally, an O_2 plasma is used to remove the thin epoxy layer remaining between the grating fingers.

Note: for technological simplicity, we did not employ alloyed Ohmic contacts. The Ti/Au contacts on the n^+ GaAs layers, thus, introduce a Schottky barrier that possibly degrades the overall QWIP performance with respect to the state-of-the-art devices. This can be overcome using low-temperature (200 °C) annealed Pd/Ge/Ti/Au Ohmic contacts on GaAs instead.[16,18,19]

Overall, the architecture, thus, consists of a symmetric MIM microcavity, embedding an ISB active region, fabricated on a mid-IR transparent support as shown in the two scanning electron microscopy (SEM) images presented in Figs. 1(b) and 1(c). The *modal* properties of the system are identical to a conventional MIM system on a continuous ground plane. The difference is in the electromagnetic coupling properties: the transparent substrate allows addressing the devices from either the top surface (hereafter called *the front side*) or through the substrate (*the back side*). We propose to call this detector with two excitation and/or collection ports for the light, a "Janus photodetector." We borrow the term from the ancient roman mythological god Janus, depicted as having two faces looking in opposite directions—its name not by chance connected directly to the meaning of "doorway."

The devices were first optically characterized using a mid-IR microscope coupled to a Fourier transform infrared (FTIR) spectrometer (Nicolet Nexus 870). The microscope permits to perform micro-reflectance (R) and micro-transmission (T) by selecting the area probed by the mid-IR beam using a pair of illumination and collection slits along the light path. Reflectivity and transmissivity spectra were obtained at room temperature, focusing and collecting light only on the $80 \times 80\ \mu$m^2 area defined by the grating with two aligned 32× Cassegrain objectives (see sketches in Fig. 2). Light impinges on

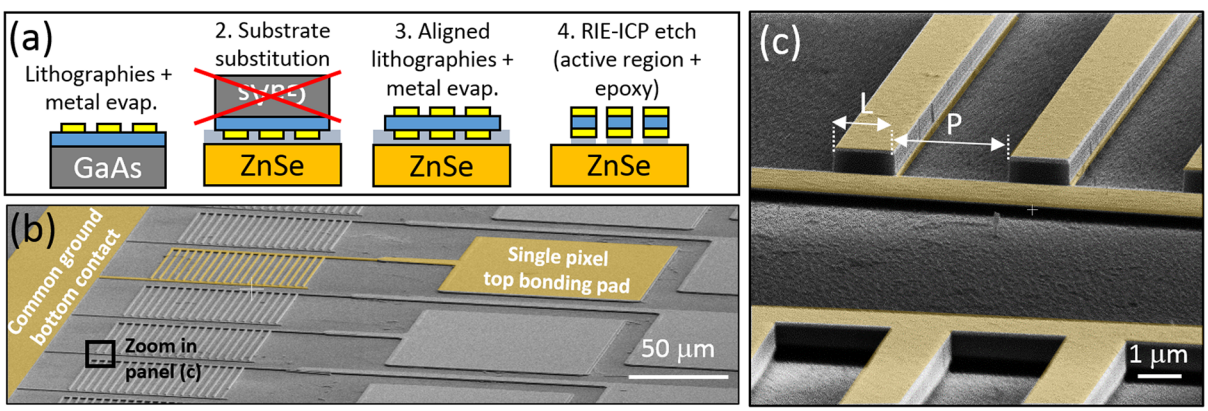

FIG. 1. (a) Main steps for sample fabrication: the active region is sandwiched in a symmetric MIM layout and bonded to a mid-IR transparent ZnSe substrate. (b) and (c) Colorized SEM images showing the sample layout: a common electrode provides ground connection to all the devices, while a dedicated bonding pad selectively addresses each pixel. The stripe width (L) varies between 0.9 and 1.35 μm, while the distance P is kept constant.

Published under an exclusive license by AIP Publishing

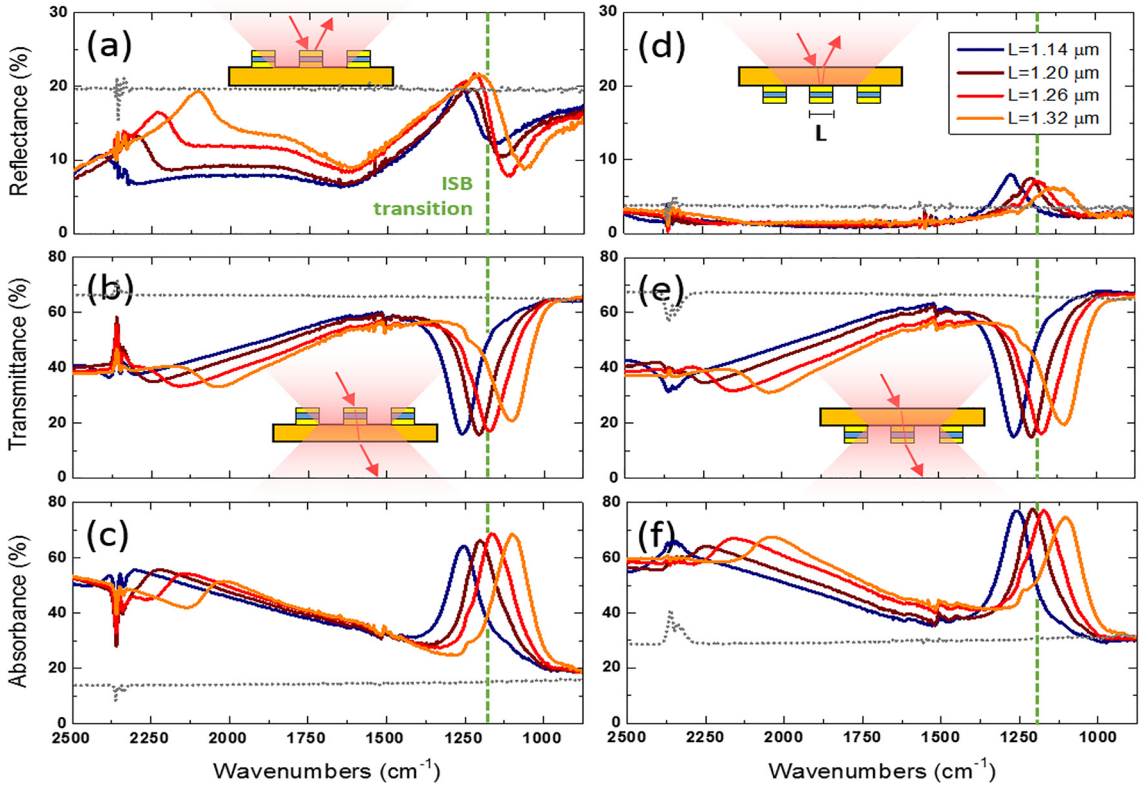

FIG. 2. Micro-FTIR passive optical characterizations for different optical cavity geometries (stripe width L varies to span the photonic resonance across the ISB transition at 1180 cm^{-1}). TM-polarized light is focused on the MIM structures with a Cassegrain objective from the top-side, collecting (a) reflectivity and (b) transmission. The same measurements are performed by rotating the sample upside down and impinging through the ZnSe substrate, focusing at the interface hosting the active region [(d) and (e)]. The absorption spectra are inferred as A = 1–R–T [panels (c) and (f)]. Dotted gray lines: spectra collected on the bare ZnSe substrate, in nearby regions; green vertical line: ISB transition (1176 cm^{-1}).

the sample with an angle of incidence of 25°–35° and is TM-polarized using a KRS5 polarizer along the optical path. The grating stripes are orthogonal to the plane of incidence. A control spectrum is collected under the same conditions on nearby, un-patterned ZnSe areas [dotted gray spectra in panels (a)–(f) of Fig. 2], to experimentally evaluate the reflectivity at the air/ZnSe interface.

Figures 2(a) and 2(b) show, respectively, the room-temperature reflectance and transmittance spectra of the MIM cavities for a selection of different stripe widths (L = 1.14, 1.20, 1.26, and 1.32 μm) with light incident from the front side. Pronounced resonant features are observed in both reflection and transmission, correctly frequency-tuning with the cavity at the change of L. We focus on the low-energy resonances between 1000 and 1400 cm^{-1}, which correspond to the TM_{01} mode of the microcavities,[20–22] relevant for the operation, and follow the equation $\lambda_{res} = 2 \times L \times n_{eff}$ (L being the width of the stripe and $n_{eff} = 3.3$ the effective refractive index of the heterostructure). The higher order TM_{02} mode in the range 2000–2500 cm^{-1} is also visible in the spectra but is not relevant for detection, as it does not interact with the ISB transition. The reflectivity spectra exhibit a characteristic dispersive line shape, while transmission spectra present a pronounced dip with a contrast of ∼40%. These lineshapes are typical of two-port systems.[23]

From R and T, we can extract the front-side illumination absorbance as A = 1–R–T [Fig. 2(c)]. The resonances of interest show an absorption magnitude of around 45%. Note that these spectra also display a large background absorption of around 20% in the region of interest. The origin of this background, that is not expected to occur in a transparent substrate, can be explained by analyzing the optical losses in spectra taken on non-patterned ZnSe (gray dots in Fig. 2). We measure a spectrally independent radiation loss of the same order of magnitude: as there is, in principle, very little absorption in ZnSe, we assign the effect to multiple internal reflections or scattering within the transparent substrate slab. Due to the finite aperture of the Cassegrain objective and the truncation of the light path by the microscope slits, part of the reflected/transmitted light is not delivered to the detector. Overall, at the cavity resonance, we measure an absorbance of around 45% once corrected for the background. Since the maximum absorption value for a thinner-than-λ, two-port system illuminated from only one side is 50%, the developed detector proves very efficient in energy harvesting.[24,25] Also to be noticed is the slanted baseline, clearly seen on the patterned structures and absent on the bare ZnSe region. FDTD numerical calculations suggest the slope is linked to the Wood anomaly introduced by the large periodicity (P = 4 μm) and the 25°–35° illumination angle. A comparison of the

Published under an exclusive license by AIP Publishing

absorption with the one-port configuration, where the heterostructure is fabricated on a continuous ground plane and the transmission channel is suppressed, is available in the supplementary material, SI-1.

The same set of measurements was performed with back-side illumination: reflectance, transmittance, and absorbance are shown in Figs. 2(d)–2(f) with very similar results. As expected by the Helmholtz reciprocity principle, the transmittance spectra are practically identical, while the reflectance differs from the front-side configuration.[26,27] An absorbance as high as 45% is measured in this back-side configuration too, after correction for the light lost by geometrical effects.

The passive optical characterizations confirm that photons can be efficiently injected in our device from both sides with very similar performances as far as the absorbed power is concerned.

Next, we turn to the DC opto-electronic characterization of the devices for both front-side and back-side illuminations. The sample is mounted on a copper block with a central hole allowing optical access also from the backside, it is wirebonded, and it is fixed on the cold finger of a liquid nitrogen-cooled, continuous-flow cryostat. It is surrounded by a cryo-shield with a 24° circular field of view (FOV) access that can be opened to expose the device to a room temperature (300 K) black body radiation or closed to characterize its electrical response in the dark. Current–voltage characteristics as a function of the sample's temperature were measured using a Keithley2461 sourcemeter.

We present in Fig. 3 the dark current (black solid lines) and the background current (exposing the device to a 300 K black body either through the front side—red dashed line—or the back side—blue dashed line). The device shown here has a stripe width $L = 1.23\ \mu m$ that sustains a cavity mode at $\lambda_{res} = 1180\ cm^{-1}$, in overlapping the ISB transition ($\lambda_{ISB} = 1176\ cm^{-1}$). Additional data for an off-resonant device ($L = 1.11\ \mu m$) are presented in the supplementary material (SI-2). As noted previously, the metallic contacts form a Schottky barrier of approximately 0.6 V [a shaded gray area in Fig. 3(a)], where the photodetection process is hampered. Current–voltage I(V) characteristics are asymmetric due to the difference in processing conditions between the top and bottom contact layers. The background current is larger than the dark current for the three reported temperatures. From the measurement at 78 K, it appears that operation under negative bias is slightly favorable as it yields a larger background to dark current ratio.

By repeating the measurements over a broader temperature range (78–300 K), it is possible to obtain an estimate of the background limited infrared photodetection temperature (T_{BLIP}) as the temperature where $I_{bkg} = 2 \times I_{dark}$. It represents the minimal cooling temperature of the device, where performances are only limited by the dark current thermal noise.

The result is reported in Fig. 3(b), as the ratio of the background current over the dark current for front and back illumination as a function of temperature. For each temperature, the operating bias is selected to maximize the background-to-dark current ratio, typically in the −1 to −1.5 V range. *De facto*, this indicates the most favorable operating conditions where the S/N ratio is the largest. From the results in Fig. 3(b), we estimate a T_{BLIP} around 200 K for both front and backside configurations. We note that this could be improved in the future with the use of Ohmic contacts.

The background-to-dark current ratio increases slightly with the temperature from 78 to 115 K before dropping rapidly below 2. This effect has been previously reported in QWIPs operating in the mid-IR and THz.[16,28,29] It originates from the extra energy necessary to promote electrons from the doped GaAs contact layers above the first QW barrier, which results in a triangular injection band profile. In our case, this phenomenon is further amplified by the presence of the Schottky barriers at the GaAs/metal interfaces. As a result, electrons need a larger energy to overcome the potential barrier and be emitted/collected from the contacts.

Finally, we discuss the photodetection response of this two-port Janus QWIP. Light coming from the internal source of an FTIR spectrometer (Bruker Vertex 70v) is focused on the device with a parabolic mirror. The sample is kept on the same support previously used and mounted in the same cryo-shielded cryostat, so to ensure that only one side of the device is exposed to external radiation. A low-noise amplifier (SR570) is used to apply an external bias on the device and amplify its current response with a typical sensitivity of 500 nA/V. The amplified signal is first fed directly into a lock-in amplifier, used to

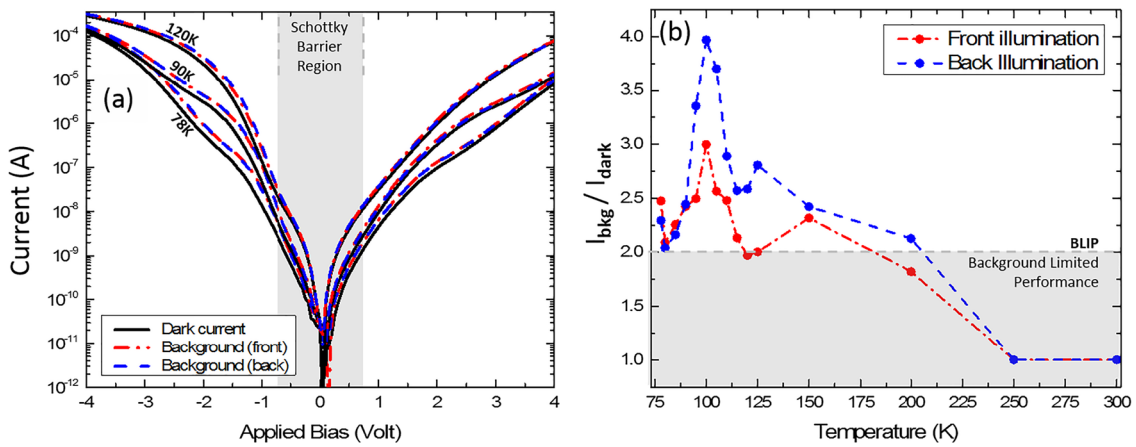

FIG. 3. (a) Current–voltage characteristics of the resonant ($L = 1.23\ \mu m$) device in the dark (black solid lines) or upon ambient temperature background illumination from the front (blue dashed line) or back (red dashed-dotted line) side. (b) Ratio of the background current to the dark current as a function of temperature showing that the operation is background limited up to around 200 K—taking into account for each temperature point the applied bias that maximizes photocurrent detection.

Published under an exclusive license by AIP Publishing

finely align the photodetector pixel on the focused spot of the incoming radiation, and then is sent back to the FTIR as "external detector signal" for spectrum acquisition in the rapid scan mode.

Following the scheme of previous experiments, we characterized the detector for the two coupling configurations—frontside and backside illumination—and collected signal from three independent pixels (stripe width L = 1.26 μm, L = 1.14 μm, and L = 1.02 μm). To complete the analysis, we collected data at different operating temperatures (for brevity, published in the supplementary material, Sec. SI-3).

Figure 4 shows the detector performance at 78 K for the three investigated pixels with photocurrent spectra normalized to the delivered power (measured with a thermopile powermeter) and the effective illuminated area (real dimensions of the focused beam determined by a knife-edge measurement). The grating with L = 1.26 μm features a photonic resonance peaked at $\lambda_{res} = 1180\ cm^{-1}$, matching the ISB transition at 1176 cm^{-1}. It shows a sharp and symmetric photodetection peak for both front-side and back-side illumination. By decreasing the value of the geometric parameter L, we explore the off resonance region, as the detection peak blueshifts accordingly. An asymmetry in the photocurrent spectrum is introduced by the blueshift of the photonic mode that modulates the spectral shape, enhancing the detection at the tail of the ISB transition. A double peaked photoresponse is observed for the grating L = 1.14 μm, and it is even more apparent for a larger detuning (L = 1.02 μm). Despite the decrease in detectivity, the bandwidth for which photocurrent is generated increases, allowing photodetection between 1000 and 1500 cm^{-1}. This evidences the large tunability of the photodetection range by changing the photonic architecture of the device. The responsivity reaches the value of 18 mA/W. Considering that the two-port configuration inherently loses half of the delivered optical energy, this is not far from the responsivity of other devices employing MIM cavities and non-annealed contacts.[30]

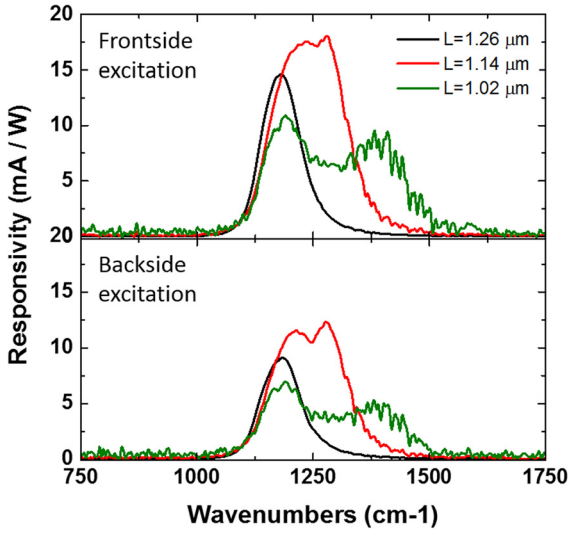

FIG. 4. Photodetector responsivity obtained at 78 K for three different devices, illuminated from the front (solid lines) or back (dotted lines) surface. All spectra are arbitrary normalized to the best performing condition (L = 1.14 μm with backside illumination).

To conclude, we have demonstrated the operation of a metal–insulator–metal cavity-enhanced QWIP on a mid-IR transparent substrate, which shows very similar performances in both direct and backside illumination. This technological innovation allows for a vast number of perspective applications that were up to now essentially not available due to the use of Au–Au thermocompression wafer bonding techniques. In the perspective, it is, in principle, now possible to process the detector in a matrix architecture with flip-chip soldering solutions that permit the use of fast, standardized electronic readout-circuits to develop a mid-IR, cavity-enhanced QWIP camera. Simultaneous two-side illumination is also a desirable feature in experiments involving, e.g., heterodyne detection schemes where a precise alignment and overlap between two beams is necessary. In the case of a single-side illumination sensor, a trade-off must be found between non-collinear alignment and the use of beam-splitters, whereas the use of a two-side illumination device allows simultaneous optical access from both sides and permits us to remove the beam splitter. This approach has been demonstrated in the THz with hot-electron bolometers,[17] but never in the mid-IR range of the spectrum. Finally, the performances of our device can be enhanced by using Ohmic contact alloys and annealing schemes, as well as more refined cavity architectures like square patch microcavities instead of a 1D stripe geometry.

See the supplementary material for the DC electrical characterization of an off resonance pixel (stripe width L = 1.11 μm, exhibiting an optical resonance at 1300 cm^{-1} and allowing a comparison with the "on-resonance" structures presented in the main text—Fig. 3) and photocurrent spectra for different operation temperatures that are attached for the sake of completeness.

We acknowledge financial support from the European Union FET-Open Grant MIR-BOSE (No. 737017) and from European Union's Horizon 2020 Research and Innovation Program, under the Marie-Skłodowska Curie Grant Agreement No. 748071. We also acknowledge financial support from the French National Research Agency, projects IRENA (ANR-17-CE24-00016) and SOLID (ANR-19-CE24-0003). This work was partly supported by the French RENATECH network.

AUTHOR DECLARATIONS

Conflict of Interest

The authors have no conflicts of interest to disclose.

DATA AVAILABILITY

The data that support the findings of this study are available from the corresponding authors upon reasonable request and its supplementary material.

REFERENCES

[1]H. C. Liu and J. Li, Appl. Phys. Lett. **67**, 1594 (1995).
[2]P. D. Grant, R. Dudek, M. Buchanan, and H. C. Liu, IEEE Photonics Technol. Lett. **18**, 2218 (2006).
[3]A. Delga and L. Leviandier, Proc. SPIE **10926**, 1092617 (2019).
[4]M. Hakl, O. Lin, S. Lepillet *et al.*, ACS Photonics **8**(2), 464 (2021).
[5]C. G. Bethea, B. F. Levine, G. Hasnain *et al.*, J. Appl. Phys. **66**, 963 (1989).
[6]D. Palaferri, Y. Todorov, A. Bigioli *et al*, Nature **556**, 85 (2018).
[7]M. F. Hainey, T. Mano, T. Kasaya *et al.*, Nanophotonics **9**(16), 4775 (2020).

Published under an exclusive license by AIP Publishing

[8]Y. Fu, M. Willander, W. Lu, and W. Xu, J. Appl. Phys. **84**(10), 5750 (1998).
[9]S. D. Gunapala, J. S. Park, G. Sarusi *et al.*, IEEE Trans. Electron Devices **44**(1), 45 (1997).
[10]S. Kalchmair, H. Detz, G. D. Cole *et al.*, Appl. Phys. Lett. **98**(1), 011105 (2011).
[11]G. Su, L. Liu, W. Zang *et al.*, IEEE Photonics Technol. Lett. **30**(13), 1167 (2018).
[12]V. Apalkov, G. Ariyawansa, A. G. U. Perera *et al.*, IEEE J. Quantum Electron. **46**(6), 877 (2010).
[13]N.-L. Tran, M. Malerba, A. Talneau *et al.*, Opt. Express **27**(2), 1672 (2019).
[14]M. Jeannin, G. M. Nesurini, S. Suffit *et al.*, ACS Photonics **6**(5), 1207 (2019).
[15]M. Jeannin, T. Bonazzi, D. Gacemi *et al.*, Nano Lett. **20**(6), 4430 (2020).
[16]M. Jeannin, T. Bonazzi, D. Gacemi *et al.*, Appl. Phys. Lett. **117**(25), 251102 (2020).
[17]F. Joint, G. Gay, P.-B. Vigneron *et al.*, Appl. Phys. Lett. **115**, 231104 (2019).
[18]L. C. Wang, P. H. Hao, and B. J. Wu, Appl. Phys. Lett. **67**(4), 509 (1995).
[19]L. C. Wang, P. H. Hao, J. Y. Cheng *et al.*, J. Appl. Phys. **79**(8), 4216 (1996).
[20]Y. Todorov, L. Tosetto, J. Teissier *et al.*, Opt. Express **18**(13), 13886 (2010).
[21]C. A. Balanis, *Antenna Theory* (John Wiley & Sons, 2005).
[22]S. Pirotta, N.-L. Tran, A. Jollivet *et al.*, Nat. Commun. **12**, 799 (2021).
[23]S. Fan, W. Suh, and J. D. Joannopoulos, J. Opt. Soc. Am. A **20**(3), 569 (2003).
[24]A. Chutinan and S. John, Phys. Rev. A **78**(2), 023825 (2008).
[25]S. Zanotto, F. Mezzapesa, F. Bianco *et al.*, Nat. Phys. **10**(11), 830 (2014).
[26]D. Jalas, A. Petrov, M. Eich *et al.*, Nat. Photonics **7**, 579 (2013).
[27]K. X. Wang, Z. Yu, S. Sandhu, and S. Fan, Opt. Lett. **38**(2), 100 (2013).
[28]H. C. Liu, R. Dudek, A. Shen *et al.*, Appl. Phys. Lett. **79**(25), 4237 (2001).
[29]H. Luo, H. C. Liu, C. Y. Song, and Z. R. Wasilewski, Appl. Phys. Lett. **86**(23), 231103 (2005).
[30]Y. N. Chen, Y. Todorov, B. Askenazi *et al.*, Appl. Phys. Lett. **104**, 031113 (2014).

Published under an exclusive license by AIP Publishing